



**HAL**  
open science

## Molecular modelling of the heat capacity and anisotropic thermal expansion of nanoporous hydroxyapatite

Tulio Honorio, Thibault Lemaire, Devis Di Tommaso, Salah Naïli

### ► To cite this version:

Tulio Honorio, Thibault Lemaire, Devis Di Tommaso, Salah Naïli. Molecular modelling of the heat capacity and anisotropic thermal expansion of nanoporous hydroxyapatite. *Materialia*, 2019, pp.100251. 10.1016/j.mtla.2019.100251 . hal-02018776

**HAL Id: hal-02018776**

**<https://hal.science/hal-02018776>**

Submitted on 22 Oct 2021

**HAL** is a multi-disciplinary open access archive for the deposit and dissemination of scientific research documents, whether they are published or not. The documents may come from teaching and research institutions in France or abroad, or from public or private research centers.

L'archive ouverte pluridisciplinaire **HAL**, est destinée au dépôt et à la diffusion de documents scientifiques de niveau recherche, publiés ou non, émanant des établissements d'enseignement et de recherche français ou étrangers, des laboratoires publics ou privés.



Distributed under a Creative Commons Attribution - NonCommercial 4.0 International License

# Molecular modelling of the heat capacity and anisotropic thermal expansion of nanoporous hydroxyapatite

Túlio Honório<sup>a,1</sup>, Thibault Lemaire<sup>a</sup>, Devis Di Tommaso<sup>b</sup>, Salah Naili<sup>a,\*</sup>

<sup>a</sup>*Université Paris-Est, Laboratoire Modélisation et Simulation Multi Echelle, MSME UMR 8208, CNRS, UPEC, UPEM, Créteil Cedex 94010, France*

<sup>b</sup>*Thomas Young Centre, Materials Research Institute and School of Biological and Chemical Sciences, Queen Mary University of London, Mile End Road, London E1 4NS, UK*

---

## Abstract

Hydroxyapatite, which is the main mineral phase of mammalian bone, occurs in the form of small bricks of colloidal size organized in a way that leaves room to micro- and mesopores. These pores are filled with an electrolyte and confined fluids are recognized for manifesting different dynamical and structural behaviors when compared to bulk fluids. Research on other nanoporous materials reported that confinement may have repercussions on the effective thermal properties of these materials. Understanding the physical origin of thermal expansion and heat capacity as a function of the hydroxyapatite porosity is, therefore, crucial to predict the thermo-mechanical behavior of bone. Molecular dynamics simulations of hydroxyapatite nanopores ( $2 \text{ nm} \leq H \leq 16 \text{ nm}$ , where  $H$  is the size of the nanopore) in contact with liquid water have been used to determine the effect of nanoporosity and water confinement on the heat capacity and thermal expansion of this important biomaterial. At temperatures corresponding to *in vivo* conditions, the thermal expansion of water confined in nanopores smaller than 6 nm is solid-like but becomes liquid-like in larger nanopores. The heat capacity of confined water exhibits a maximum at pore sizes of approximately 7 nm. An up-scaling strategy taking

---

\*Corresponding author

<sup>1</sup>*Present address:* LMT-Cachan/ENS-Cachan/CNRS/Université Paris Saclay, Cachan, France

into account the anomalous behaviour of nanoconfined water is then proposed to determine the effective heat capacity and the effective heat of hydroxyapatite expansion as a function of its porosity, and to predict regions of variability, compared with the bulk, in the thermal properties of porous hydroxyapatite.

*Keywords:* Hydroxyapatite; Confined water; Thermal expansion; Specific heat; Molecular dynamics; Homogenization.

---

## 1. Introduction

Properties such as thermal expansion and heat capacity characterize the behavior of mammalian bone under varying temperature conditions. In fact, despite it is often assumed that bone is subject to small temperature variations, even subtle differences between the bone surface and deep-body zone temperatures might impact the local metabolism [1]. Moreover, orthopedic [2, 3, 4, 5] and odontological [6] interventions can to produce significant thermal effects. For instance, Jacobs et al. [6] observed temperature rises of at least 5°C in both graft bed and bone with dental burrs, and Krause et al. [3] reported clinical tests during total joint replacement operations in which temperatures exceed 200°C when irrigation was not used. Temperatures above 45°C were reported to cause thermal osteonecrosis [4, 5]. The recognition of the importance of these thermal effects goes back to Hippocrates' recommendation (500 BC) of frequently plunging the tools into cold water when trephining discs of bone from the skull to prevent the heating of the material [2, 7]. Healing following bone surgery may be delayed if the bone cells are injured by thermal effects [8]. From another perspective, thermal stimulation of tissues aiming at inducing localized necrosis has been proposed as a therapeutic tool [9]. However, relatively few experimental and theoretical studies have been concerned with the thermal properties of bone.

As the main constituent inorganic phase of mineralized tissue found in mammalian bone, tooth enamel and dentin, Hydroxyapatite (HAP),  $\text{Ca}_{10}(\text{PO}_4)_6(\text{OH})_2$ , can be used as a proxy to study the thermal properties of bone. In these tissues,

HAP occurs in the form of small ‘bricks’ of colloidal size [10, 11] organized in  
25 a way that leaves room to pores sizes ranging from 2 to 24 nm [12] in contact  
with body fluid. This was for example showed using high resolution transmission  
electron microscopy (TEM) and electron diffraction as well as 3D stereoscopic  
TEM [10], and further confirmed by atomic force microscopy [11]. Confined  
water manifests different dynamical and structural behaviors when compared  
30 to bulk fluids (e.g. [13]), and research on other porous materials showed that  
nanoconfinement may have repercussions on their effective thermal properties  
[14, 15, 16, 17, 18, 19].

The molecular dynamics (MD) simulation technique is particularly suited to  
assess the behavior of water confined in nanopores as it allows the quantification  
35 of interatomic forces and atomistic phenomena responsible for the anomalous  
behaviour of water, which otherwise would be difficult to probe experimentally,  
especially at the temperature and pressure corresponding to *in vivo* conditions  
[20]. Recent works of the authors using MD revealed important aspects of the  
structure and dynamics of water in HAP-water nanopores [21, 22, 23, 24], in-  
40 cluding the mechanisms controlling the anisotropic diffusion of water molecules  
within nanopores [25].

We anticipate that nanoporosity could also have a significant effect on the  
thermal properties HAP, but despite its importance in biomechanic applications,  
to the best of the authors’ knowledge, no experimental or theoretical data is  
45 available regarding the role of nanoporosity on the thermal expansion and heat  
capacity. In this work, the MD technique has been applied to compute the  
thermal expansion and heat capacity of bulk HAP and HAP-water nanopores  
with pore sizes ranging from 2 to 16 nm, and to quantify the effect of water  
nanoconfinement on the thermal properties of hydroxyapatite. An upscaling  
50 strategy based on homogeneization techniques is then used to link the anomalous  
thermal behaviour in HAP-water nanopores to the effective thermal expansion  
and effective heat capacity of HAP, as a function of its porosity.

## 2. Methods

### 2.1. Heat capacity and thermal expansion from molecular dynamics simulations

At the nanoscopic level, the heat capacity of a material is related to the vibrational modes of atoms (phonons) and the thermal expansion to the anharmonicity of the lattice interaction potential [26]. The heat capacity at constant strain  $C_\epsilon$  quantifies how the internal energy  $U$  changes with temperature  $T$ :

$$C_\epsilon = \left( \frac{\partial U}{\partial T} \right)_{\epsilon_{ij}}, \quad (1)$$

where  $\epsilon_{ij}$  are the components of the second-order Lagrangian deformation tensor  $\boldsymbol{\epsilon}$  which is symmetric and associated with a reference volume  $V_0$ . In this paper, we adopt the convention that the subscripts as  $i, j$  and  $k$ , which vary from 1 to 3, correspond to the Cartesian coordinates  $\mathbf{x}, \mathbf{y}$  and  $\mathbf{z}$ , respectively (see Fig. 1). So, the indices 1, 2 and 3 map to  $\mathbf{x}, \mathbf{y}$  and  $\mathbf{z}$  respectively. For a unit cell, the deformation tensor is defined by:

$$\boldsymbol{\epsilon} = \frac{1}{2} [\mathbf{h}_0^{-T} \mathbf{h}^T \mathbf{h} \mathbf{h}_0^{-1} - \mathbf{I}], \quad (2)$$

55 where  $\mathbf{h}_0$  and  $\mathbf{h}$  are two tensors associated with the metric of the reference and deformed unit cell, respectively,  $\mathbf{I}$  is the unit tensor, and the superscript  $[\star]^T$  denotes the transpose operator. Note that the unit cell is periodically repeated to fill all space whose the form and the volume are completely arbitrary but described by the 3 vectors  $\mathbf{a}, \mathbf{b}$  and  $\mathbf{c}$  that span the edges of the unit cell. This  
60 description can be obtained by arranging the vectors as  $\{\mathbf{a}, \mathbf{b}, \mathbf{c}\}$  to form a (3,3) matrix  $\mathbf{h}$  whose the columns are the components of  $\mathbf{a}, \mathbf{b}$  and  $\mathbf{c}$  (see Fig. 1) in this order.

The heat capacity at constant stress  $C_\sigma$  quantifies how the enthalpy changes with the temperature:

$$C_\sigma = \left( \frac{\partial H}{\partial T} \right)_{\sigma_{ij}} = \left( \frac{\partial(U + V_0 \text{Tr}(\boldsymbol{\sigma} \boldsymbol{\epsilon}))}{\partial T} \right)_{\sigma_{ij}}, \quad (3)$$

65 where  $\boldsymbol{\sigma}$  is the second-order Cauchy stress tensor which is symmetric and whose the components are denoted by  $\sigma_{ij}$  [27, 28, 29, 30] and  $\text{Tr}$  denotes the trace

operator of a tensor. The second-order thermal expansion tensor  $\alpha$ , which is symmetric and defined by these components  $\alpha_{ij}$ , quantifies how the strain changes with the temperature under a constant stress:

$$\alpha_{ij} = \left( \frac{\partial \epsilon_{ij}}{\partial T} \right)_{\sigma_{ij}}. \quad (4)$$

70 The heat capacities  $C_\sigma$  and  $C_\epsilon$ , and the elements of the thermal expansion tensor are related by the following expression [31]:

$$C_\sigma - C_\epsilon = V_0 T C_{ijkl} \alpha_{ij} \alpha_{kl}, \quad (5)$$

where  $C_{ijkl}$  is the fourth-order elastic stiffness tensor which is symmetric. In this paper, the Einstein summation convention is used which implies a summation over a set of indexed terms in a formula.

75 The heat capacities and the thermal expansion tensor have been computed from MD simulations using the fluctuation-dissipation formula. The fluctuation of two dynamical variables  $A$  and  $B$  is given by  $\langle \delta A \times \delta B \rangle_{ens} = \langle AB \rangle_{ens} - \langle A \rangle_{ens} \langle B \rangle_{ens}$ , where the operator  $\langle \delta \star \rangle_{ens}$  denotes an ensemble average. In the isotension-isothermal ( $N\sigma T$ ) ensemble, the constant stress heat capacity can be  
80 computed from the fluctuations of the enthalpy  $H$  [32]:

$$C_\sigma = \frac{\langle \delta H^2 \rangle_{N\sigma T}}{kT^2}, \quad (6)$$

where  $k$  is the Boltzmann constant. In the isotension-isothermal ( $N\sigma T$ ) ensemble, the thermal expansion tensor can then be computed from the cross fluctuations of the strain and the enthalpy [27, 28, 30]:

$$\alpha_{ij} = \frac{\langle \delta \epsilon_{ij} \times \delta H \rangle_{N\sigma T}}{kT^2}. \quad (7)$$

The heat capacity at constant strain  $C_\epsilon$  can then be computed using Eq. (5).  
85 Fluctuation-dissipation formula are particularly advantageous if one is interested in compute various properties or tensorial properties from a single simulation.

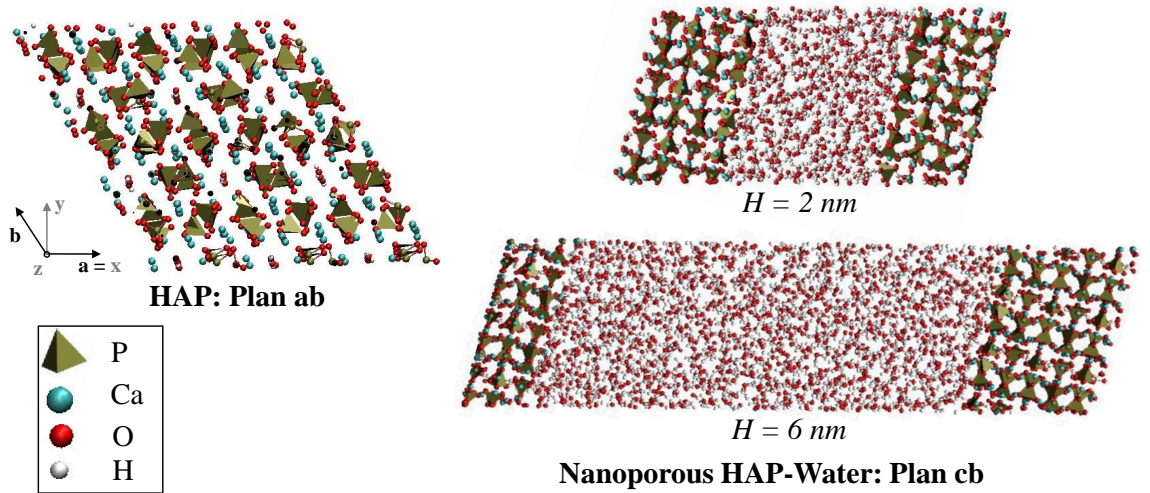


Figure 1: Snapshot of configuration of bulk HAP and HAP-water systems with  $H = 2$  nm and  $H = 6$  nm. For reference, the Cartesian coordinates ( $x, y, z$ ) and crystallographic ( $a, b, c$ ) frames are also shown.

## 2.2. Simulation details

The atomic structure of HAP was obtained from the hexagonal with  $P6_3/m$  space group cell parameters of Sudarsanan and Young [33]. The simulation box is generated by stacking this unit cell 3 times in each in-plane direction and 4 times in out-of-plane direction (see Fig. 1), which results in a total number of atoms in the HAP solid layer of  $N_{HAP} = 1584$  atoms.

For simulation of nanoporous HAP-water systems, HAP platelets were stacked with a surface-to-surface spacing along  $c$ -direction varying from 2 to 16 nm. The  $\{0001\}$  surface of HAP, which is the dominant surface in the thermodynamically-stable morphology [34], was considered as the basal plane. The slit pore was filled with water molecules at an experimental density of  $1 \text{ g.cm}^{-3}$ , which is close to the density of SPC/E water at ambient conditions.

The interatomic potential proposed by de Leeuw and co-workers [35, 36] to model crystalline apatite was used for HAP. In this force field, non-bonded interactions are described by Buckingham potentials, phosphate and hydroxyl group bonds as the sum of a Morse and a Coulombic potential, and phosphate bond

angles by a harmonic potential. The polarizability of oxygen anion in the phosphate and hydroxyl groups is described by a core-shell model. In HAP-water systems, water were modeled using the extended single-point charge (SPC/E) water model [37], and HAP-water interactions were described using non-bonded potentials derived in previous MD studies [38, 39].

MD simulations were performed using DL\_POLY 4.05.1 code [40]. The systems were first equilibrated in the microcanonical (NVE) ensemble for 1 ns. Then, a first isotension-isothermal ( $N\sigma T$ ) run during 1ns was performed to equilibrate the system under a pressure of 1 atm and at a fixed temperature (from 290 to 330 K). The Nosé-Hoover thermostat and barostat, at relaxation time 500 fs for both, were used. Smoothed Particle Mesh Ewald (SPME) method with the acceptable relative error of  $10^{-6}$  were employed to compute the long-range electrostatic interactions.

In order to verify the convergence of the estimations of the heat capacity and coefficients of thermal expansion, in the production phase the system was sampled for 2 ns in  $N\sigma T$  ensemble (timestep of 1 fs). Figure 2 displays the fluctuations of the enthalpy, volume and deformations according to the in- and out-of-plane directions. To compute the deformations, the reference cell parameters defined via  $\mathbf{h}_0$  (see Eq. (1)) were determined from the average at zero tension in  $N\sigma T$  ensemble (*i.e.* in a state in which the deformation vanishes [41]). After approximately 1 ns the fluctuations yield smooth Gaussian distributions as shown in Fig. 2. From the estimations of the heat capacity, the isothermal compressibility and the coefficients of thermal expansion, we assume that a simulation run of 1 ns in isotension-isothermal ensemble captures the normal distribution of the thermodynamic quantities (**a**)-(**c**) and is enough to converge the results of the computed properties (**d**)-(**f**).

In this study, the pore size  $H$  is defined as the projection of  $\mathbf{c}$  vector on the  $\mathbf{z}$ -direction minus the effective thickness  $h_{HAP}$  of the solid HAP [21]. Following the definition of effective thickness and pore size used for other layered materials [42],  $h_{HAP}$  is defined as the distance between the center of the out-most oxygen (the out-most species in HAP surface) in each exposed HAP sur-

Table 1: Details of HAP-water systems. The number of atoms in HAP solid layer is  $N_{HAP} = 1584$ .

$H$ (nm)	$\langle H \rangle$ (nm)	$N_w$
2	1.86	455
3	2.98	682
4	3.83	910
6	6.11	1363
8	7.97	1823
10	10.09	2276
12	12.16	2732
16	16.73	3650

135 face projected on  $\mathbf{z}$ -direction plus twice the van der Waals radius of oxygen ( $r_O = 0.152$  nm). Correspondingly, the average pore size  $\langle H \rangle_{N\sigma T}$  is computed by:  $\langle H \rangle = \langle \mathbf{c} \cdot \mathbf{z} \rangle_{N\sigma T} - \langle h_{HAP} \rangle_{N\sigma T}$ . Table 1 displays the number of water molecules  $N_w$  for each target pore size  $H$ .

### 140 3. Results

#### 3.1. Bulk HAP

Table 2 reports the heat capacity  $C_\sigma$ , the coefficients of the thermal expansion tensor  $\alpha_{ii}$ , and the isothermal compressibility  $\kappa$  of bulk HAP computed from MD simulations at 300 K and compared to theoretical and experimental values reported in the literature. To obtain further validation of our atomistic model, we also computed the components of elastic stiffness tensor using the Parinello-Rahman fluctuation equation [43]:

$$C_{ijkl} = \frac{kT}{\langle V \rangle_{N\sigma T}} [\langle \delta\epsilon_{ij} \times \delta\epsilon_{kl} \rangle_{N\sigma T}]^{-1}.$$

The representation adopted in this paper is called the Voigt's representation in which the new indexes I et J vary in the set  $\{1, \dots, 6\}$  such as  $I = (i, j)$  and

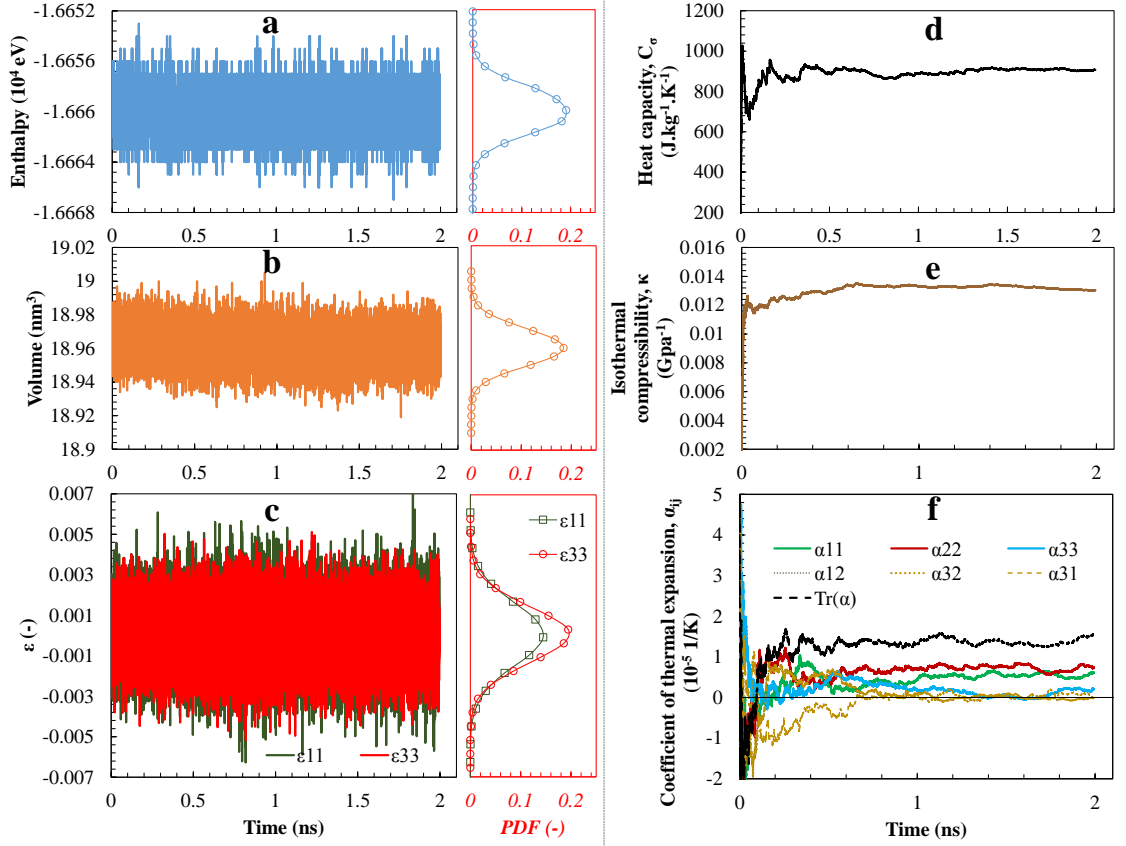


Figure 2: Convergence of thermodynamic quantities in bulk HAP at 310 K and under 1 atm. At left, the fluctuations of the (a) enthalpy, (b) volume, and (c) deformation along the  $x$  (11) and  $z$  (33) directions. At right, the variation of the (d) heat capacity, (e) isothermal compressibility (obtained from the fluctuations of the volume by [32]:  $\kappa = \frac{\langle V^2 \rangle N \sigma T}{k T V}$ ), and (f) coefficients of thermal expansion. For the latter, all components of the tensor  $\alpha$ , computed from the fluctuations of the deformations with Eq. (7) as well as its trace are reported shown.

Table 2: Heat capacity  $C_\sigma$ , coefficients of the tensor of thermal expansion  $\alpha_{ii}$  and isothermal compressibility  $\kappa$ , and components of stiffness tensor  $C_{11}$ ,  $C_{22}$  and  $C_{33}$  (Voigt notation) of bulk HAP at 300 K and under 1 atm. For comparison, results from the literature concerning, except otherwise indicated, experimental evaluation of hexagonal HAP at 300 K are provided.

	This work	Other works
$C_\sigma$ (J.kg <sup>-1</sup> .K <sup>-1</sup> )	875±72	768 [44]; 765 (298 K) [45] 690 (MD 298 K) [46] 632 (MD monoclinic 298 K) [46]
$\alpha_{11}$ (×10 <sup>-5</sup> K <sup>-1</sup> )	0.68±0.50	0.39 [47]
$\alpha_{22}$ (×10 <sup>-5</sup> K <sup>-1</sup> )	1.38±0.81	-
$\alpha_{33}$ (×10 <sup>-5</sup> K <sup>-1</sup> )	1.31±0.32	1.86 [47]
$(1/3) \times \text{Tr}(\boldsymbol{\alpha})$ (×10 <sup>-5</sup> K <sup>-1</sup> )	1.13±1.01	1.82 (monoclinic 298 K) [48]
$C_{11}$ (GPa)	97	140.0 [49] (ab initio); 117.1 [50]; 166.7 [51]; 115 [52]; 135 [53]
$C_{22}$ (GPa)	93	134.8 [49] (ab initio)
$C_{33}$ (GPa)	120	174.8 [49] (ab initio); 231.8 [50]; 139.6 [51]; 125 [52]; 172 [53]
$\kappa$ (GPa <sup>-1</sup> )	0.013±0.004	0.0118 [49] (ab initio); 0.012 [50]; 0.016 [52]; 0.011 [53]

$J = (k, l)$  where the indices  $i, j, k$  and  $l$  vary in the set  $\{1, \dots, 3\}$ . The relation  
145 between these indices is the following  $1 = (1, 1), 2 = (2, 2), 3 = (3, 3), 4 =$   
 $(2, 3), 5 = (1, 3)$  and  $6 = (1, 2)$ .

There is a general good agreement between the properties obtained from our  
simulations and the experimental values, which corroborates the transferability  
of the empirical force fields for HAP proposed by de Leeuw and co-workers  
150 [35, 36] for the computation of thermal properties.

Figure 3 shows the temperature dependence of the heat capacity at constant  
stress  $C_\sigma$ , isothermal compressibility  $\kappa$ , and elastic stiffness constants  $C_{11}, C_{22}$   
and  $C_{33}$  (Voigt notation) of bulk HAP under 1 atm. In the range of temperature  
considered (290 up to 330 K), which correspond to *in vivo* conditions, these  
155 properties can be treated as constant.

On the other hand, in the same temperature range the diagonal elements  
of thermal expansion tensor,  $\alpha_{ii}$ , display a significant temperature dependence,

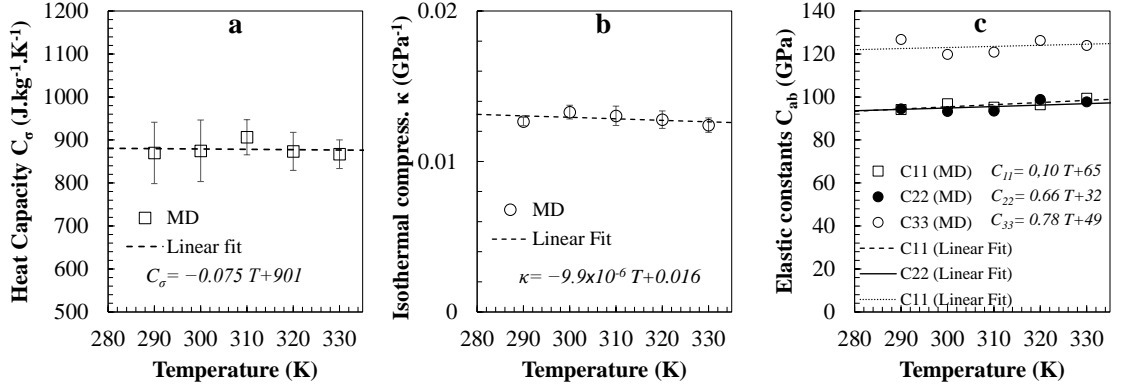


Figure 3: Temperature dependence of (a) the heat capacity at constant stress  $C_\sigma$ , (b) the isothermal compressibility  $\kappa$  and (c) the elastic constants  $C_{11}$ ,  $C_{22}$  and  $C_{33}$  (Voigt notation) under 1 atm.

as shown in Fig. 4 (a). The inset in Fig. 4 (a) shows the principal directions of the tensor of thermal expansion computed from the eigenvalues of  $\alpha$ . In a comparison with the values of the coefficients of thermal expansion in the  $\mathbf{x}$  (11),  $\mathbf{y}$  (22) and  $\mathbf{z}$  (33) directions, it can be inferred that these are the principal directions, as expected for a crystal with hexagonal symmetry. This observation is corroborated by Fig. 2 (f), where the off-diagonal terms of the thermal expansion tensor fluctuate around zero after approximately 1 ns, *i.e.* when the simulation converges.

We observe thermal contraction for temperatures exceeding approximately 315 K. The origin of this thermal contraction can be attributed to specific vibration modes observed in layered crystals. The Grüneisen parameter  $\gamma_{G,ij}$  quantifies the anharmonicity of the interactions in crystals and can be computed from the heat capacity,  $C_\sigma$ , the thermal expansion,  $\alpha_{ij}$ , and the elastic stiffness constants,  $C_{11}$ ,  $C_{22}$  and  $C_{33}$  (Voigt notation) [54]:

$$\gamma_{G,ij} = \frac{V}{C_\sigma} C_{ijkl} \alpha_{kl}. \quad (8)$$

For hexagonal crystals, there are only two independent Grüneisen parameters [55]: the in-plane  $\gamma_{G,11} = \gamma_{G,22}$  and the out-of-plane  $\gamma_{G,33}$  parameters (the

basal plane is defined with respect to the  $\{0001\}$  surface). In fact, the results  
 175 in Fig. 4 (b) shows that the in-plane Grüneisen parameter are approximately  
 equal. On the other hand, the out-of-plane  $\gamma_{G,33}$  parameter is larger between  
 290 and 300 K, where there is greater anharmonicity in the  $\mathbf{z}$ -direction than  
 in-plane directions. At 310 K, the anharmonicity in all direction are similar and  
 between 320 and 330 K the in-plane direction displays greater anharmonicity  
 180 than the out-of-plane direction. In Fig. 5, the pair distribution functions of  
 HAP computed at 290 and 300 K suggest that the thermal contraction in bulk  
 HAP is associated with a slightly increase of the inter-atomic distances between  
 the hydroxyl oxygens (c), and between the phosphate oxygens (d).

Negative Grüneisen parameters have been observed in layered crystals, due  
 185 to membrane effects [56], and in amorphous minerals [57], and they can be  
 attributed to a lateral compression following a strong expansion in the nor-  
 mal direction; this corresponds to Poisson's compression [58]. Non-monotonous  
 thermal expansion coefficients of HAP- $\beta$ -tricalcium phosphate ceramics have  
 also been reported in experiments [47].

### 190 3.2. HAP-water nanopores

Figure 6 reports the heat capacities at constant stress,  $C_\sigma$ , of nanoporous  
 HAP-water systems as a function of the pore size  $H$ , computed at conditions  
 of 310 K and 1 atm. The continuous red line corresponds to results obtained  
 using the mixture rule:

$$C_\sigma = f_{HAP}C_{\sigma,HAP} + (1 - f_{HAP})C_{\sigma,W},$$

where  $C_{\sigma,HAP} = 906 \text{ J.kg}^{-1}.\text{K}^{-1}$  (see Tab. 2) and  $C_{\sigma,SPC/E} = 4513 \text{ J.kg}^{-1}.\text{K}^{-1}$   
 [59] are the bulk values of bulk HAP and SPC/E water (dashed line) at 310 K,  
 respectively, and  $f_{HAP}$  is the volume fraction of solid HAP computed from the  
 average pore size (see Section 2.2):

$$f_{HAP} = 1 - \phi = 1 - \frac{\langle H \rangle}{\|\mathbf{c}\|},$$

where is  $\phi$  the porosity.

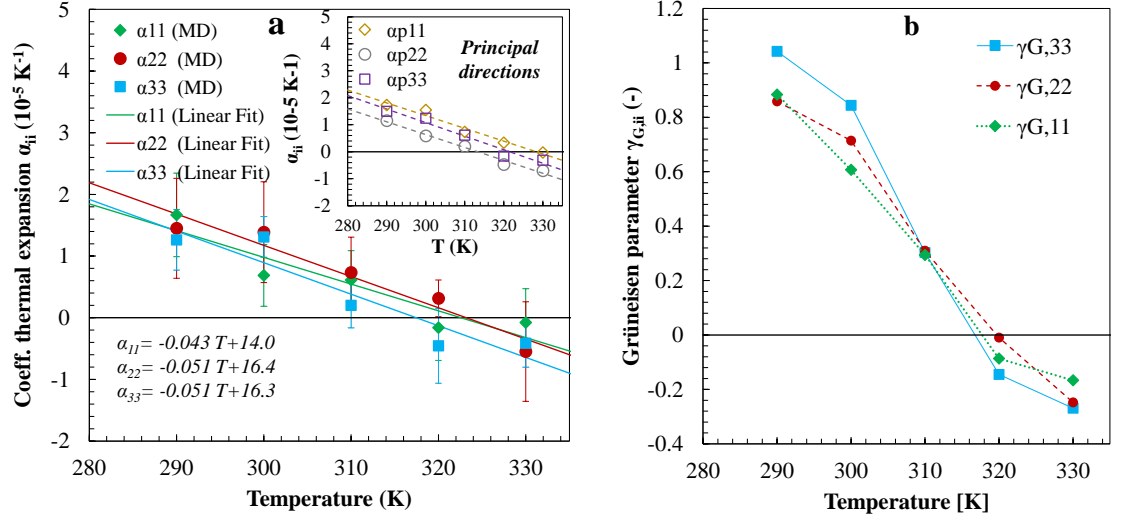


Figure 4: Temperature dependence of (a) the coefficients of thermal expansion and (b) the Grüneisen parameters of bulk HAP under 1 atm. The inset shows the principal values  $\alpha_{p,11}$ ,  $\alpha_{p,22}$  and  $\alpha_{p,33}$  of the coefficient of thermal expansion.

The heat capacity of nanoporous HAP computed from the MD simulations,  $C_{\sigma}^{MD}$ , is larger than the values estimated from the mixture rule with heat capacity of bulk HAP and SPC/E water. Consequently, confinement significantly  
 195 alters the heat capacity of water.

Using the  $C_{\sigma}^{MD}$  values computed from MD simulations, we estimated the heat capacity of confined water  $C_{\sigma,conf}$  using the mixture rule

$$C_{\sigma,conf}^w = \frac{(C_{\sigma}^{MD} - f_{HAP}C_{\sigma,HAP})}{(1 - f_{HAP})}, \quad (9)$$

(dotted blue line in Fig. 6). The heat capacity of confined water reaches a maximum for the pore size of 6 nm. This non-monotonous variation is closed  
 200 to the to value of 7 nm measured experimentally in nanoporous silica [14, 15] and, according to Etzler and co-workers [16], is due to the bimodal distribution of single molecules enthalpies in liquid water [14, 15].

When compared with the bulk, the excess of the heat capacity of confined water is on the order of  $1000 \text{ J.kg}^{-1}.\text{K}^{-1}$ . The effects of confinement on the

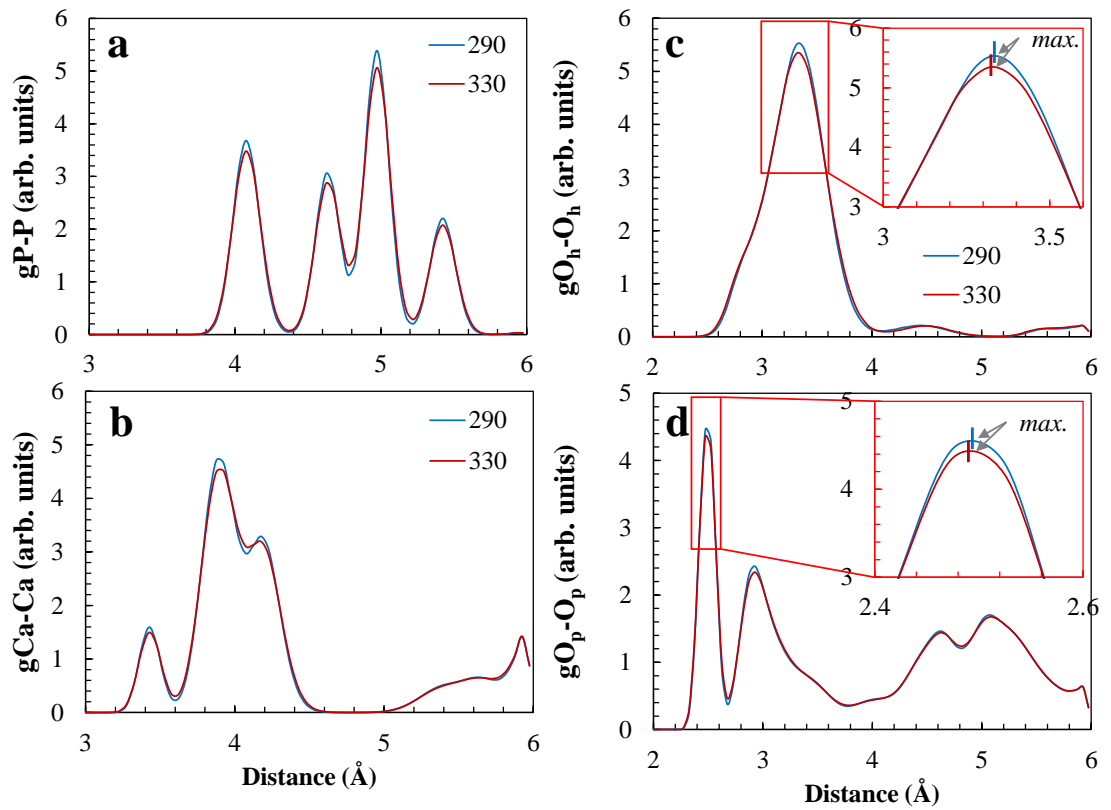


Figure 5: Radial distribution functions  $g$  of (a) P-P, (b) Ca-Ca, (c) Oh-Oh (hydroxyl oxygen) and (d) Op-Op (phosphate oxygen) pairs in bulk HAP at 290 and 330 K both under 1 atm. The insets show the distance of the peaks in the  $g$  profiles of oxygen decreasing with the temperature.

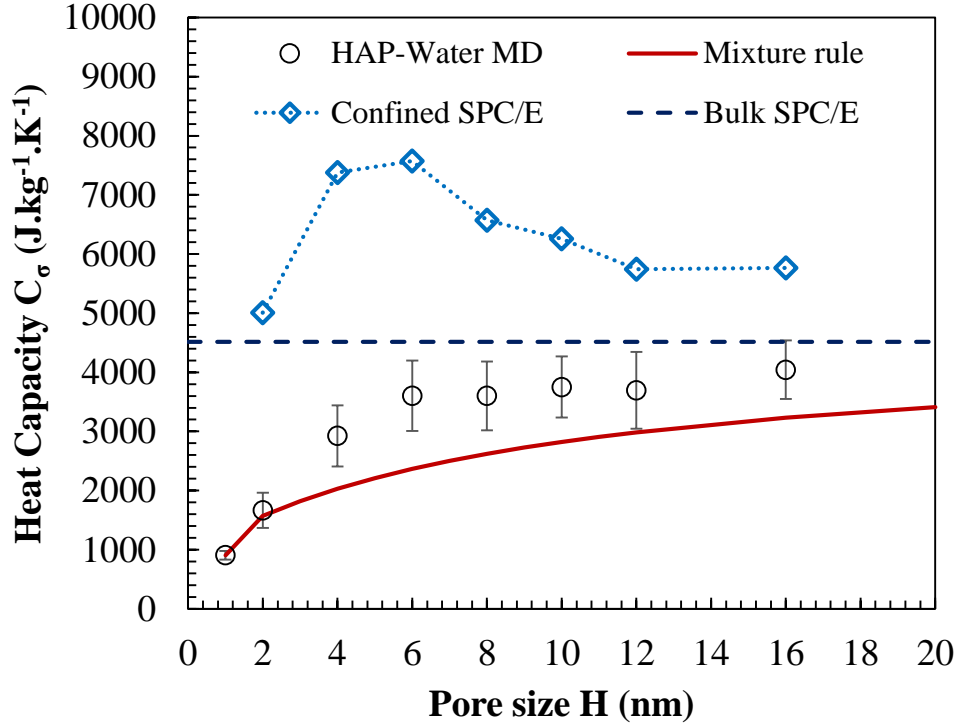


Figure 6: Heat capacity at constant stress  $C_\sigma$  of nanoporous HAP-water systems as a function of the pore size  $H$  within *in vivo* (310 K and 1 atm) conditions. Full lines display the results of a mixture rule with the bulk values of the heat capacity of HAP at 310K of  $C_{\sigma,HAP} = 906 \text{ J.kg}^{-1}.\text{K}^{-1}$  and SPC/E water (dashed line) of  $C_{\sigma,SPC/E} = 4513 \text{ J.kg}^{-1}.\text{K}^{-1}$  [59]. The dotted line display the estimations of the heat capacity of confined water  $C_{\sigma,conf}$  computed from the mixture rule:  $C_{\sigma,conf} = (C_\sigma - f_{HAP}C_{\sigma,HAP}) / (1 - f_{HAP})$ .

205 heat capacity of water in nanoporous HAP are not negligible and, therefore, are critical in relevant upscaling modeling approaches.

The coefficients of thermal expansion of HAP-water systems computed at the conditions of 310 K and 1 atm are presented in Fig. 7 as a function of the pore size  $H$ . As observed in nanoporous silica [17], the thermal expansion of confined  
 210 water also depends on the pore size. Here, we also observe that the thermal expansion in the out-of-plane direction is close to the thermal expansion of bulk HAP to pore sizes  $H$  up to 6 nm. In this case, nanoporous HAP exhibits a out-

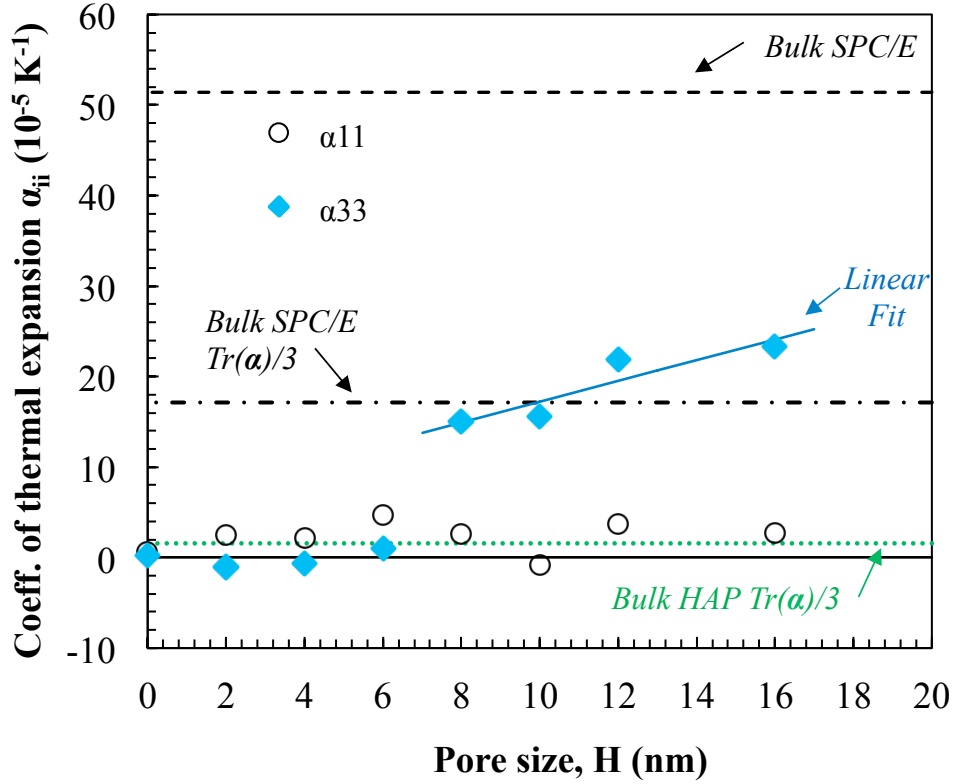


Figure 7: Coefficients of thermal expansion of nanoporous HAP-water systems as a function of the pore size  $H$  within *in vivo* (310 K and 1 atm) conditions.

of-plan thermal expansion typical of a solid close to  $10^{-5} \text{ K}^{-1}$ . On the other hand, larger pores exhibit the thermal expansion in the out-of-plane direction governed by the thermal expansion of water. In this case, nanoporous HAP exhibits a out-of-plan thermal expansion typical of a liquid like water close to  $10^{-4} \text{ K}^{-1}$ . This dependence of the thermal expansion on the pore size is likely to impact the macroscopic (effective) thermal expansion of HAP-rich materials and may be used to explain non-linearities in the thermal expansion observed experimentally in porous HAP [60].

### 3.3. Upscaling the Heat Capacity and Thermal Expansion of HAP

In this section, we present an upscaling strategy to determine the effective heat capacity and effective thermal expansion of porous HAP using as input parameters the heat capacities and the thermal expansion coefficients obtained using MD simulations of HAP-water nanopores.

The heat capacity can be extrapolated from other water contents by a rule of mixture because volume (or mass for specific heat capacities) and energy are extensive thermodynamic quantities. However, the significant dependence of the heat capacity on the pore size raises the issues of which value should be adopted in the upscaling procedure. Figure 8 (a) shows the domain of variability of the effective heat capacity of porous hydroxyapatite as a function of the porosity at 310 K and under 1 atm. The the heat capacities of bulk water and of confined water within the 6 nm HAP nanopore were used to define the lower- and upper limits of this domain.

Up-scaling the coefficient of thermal expansion is more complicated than a simple rule of mixture due to the tensorial nature of this property and the dependence on the microstructure. Analytical homogenization techniques present a consistent framework to upscale various intensive quantities and transformation fields resulting of temperature changes [61]. Here, we adopt the simple Voigt ( $\alpha_V^{eff}$ ) and Reuss ( $\alpha_R^{eff}$ ) formulas to estimate the effective coefficient of thermal expansion [62]:

$$\alpha_V^{eff} = \left\langle \frac{1}{9K_V} C_{p,ijkl} \alpha_{p,kl} \right\rangle_{\Sigma}, \text{ where } K_V = \left\langle \frac{1}{9} C_{ijij} \right\rangle_{\Sigma}, \quad (10)$$

$$\alpha_R^{eff} = \left\langle \frac{1}{3} \text{Tr}(\boldsymbol{\alpha}_p) \right\rangle_{\Sigma}, \quad (11)$$

where the subscript  $p$  stands for a phase in the composite and the operator  $\langle \star \rangle_{\Sigma}$  stands for a volume average over the representative elementary volume  $\Sigma$ . Voigt and Reuss estimations assume constant strains and constant stresses, respectively. These estimates correspond to the bounds of the effective properties

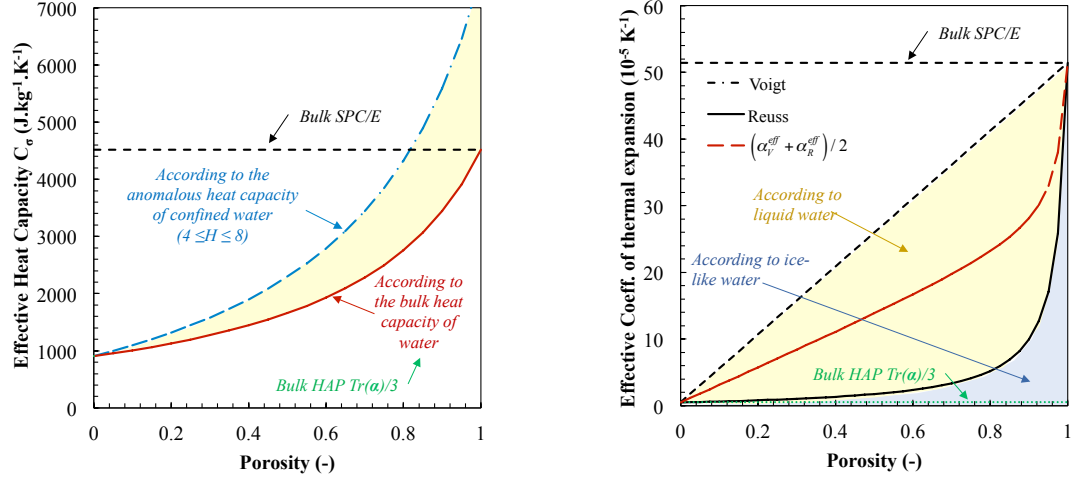


Figure 8: Estimations of the effective (a) heat capacity at constant stress and (b) the coefficients of thermal expansion of saturated HAP-water systems as a function of the porosity at  $T = 310$  K and  $P = 1$  atm conditions.

of composites. Figure 8 (b) displays the domain of variability of the effective coefficients of thermal expansion as a function of the porosity according to these limities, and the particularities of the thermal expansion of confined water within *in vivo* conditions.

#### 250 4. Discussion

*Capturing the physical origin of the heat capacity and thermal expansion of bulk HAP.* The heat capacities computed from MD simulation and fluctuation formulas are in agreement with experimental values reported for solid HAP. This corroborates the transferability of HAP empirical force fields proposed by  
 255 de Leeuw and co-workers [35, 36] to compute the thermal properties of this material. The anisotropic nature of the thermal expansion of bulk HAP was quantified at temperatures corresponding to *in vivo* conditions, and negative (principal) coefficients of thermal expansion of bulk HAP were observed for temperature exceeding 310 K. This represents the first observation of thermal

260 contraction of HAP at temperatures relevant to *in vivo* conditions.

*Nanoconfinement affects the heat capacity and thermal expansion of HAP-water.* HAP-water nanoporous systems have an effective heat capacity that exceeds the estimates obtained using the heat capacity of bulk water. Our predictions show a non-monotonous behavior for the heat capacity of confined water with a maximum value for a pore of approximately 7 nm, which is in agreement with the  
265 heat capacities obtained for other nanoporous materials [16]. The differences between the heat capacities of bulk water and of water confined in the 7 nm nanopore is very large ( $1000 \text{ J.kg}^{-1}.\text{K}^{-1}$ ) and could be the origin of the variability of macroscopic heat capacity observed experimentally in HAP-rich materials. Similarly, the thermal expansion of confined water exhibited a dependence on  
270 the confinement. The coefficients associated with the thermal expansion of HAP-water nanoporous system in the out-of-plane direction are close to the thermal expansion of bulk HAP (close to  $10^{-5} \text{ K}^{-1}$ ) up to nanopores of 6 nm; for larger pores the out-of-plane thermal expansion coefficients corresponds to the the thermal expansion of bulk water (close to  $10^{-4} \text{ K}^{-1}$ ). This dependence  
275 on the confinement is expected to impact the macroscopic (effective) thermal expansion of HAP-rich materials.

*Nanoscale origin of the variability of thermal properties in porous HAP.* Homogenization techniques were used to upscale the heat capacity and the coefficients  
280 of thermal expansion of HAP-water nanoporous. The anomalous behavior of confined water leads to significant variability at the macroscopic scale in the thermal properties of HAP materials. This finding indicates that nanoscale processes such as the confinement dependency of water properties are crucial to understand and quantify the variability of properties observed in HAP-rich  
285 materials as well as other nanoporous materials. Further, since the confined water properties are pore-size related, experimental measurements of heat capacity and coefficient of thermal expansion provide information on the micro- and mesopore size distributions in HAP.

## 5. Conclusion

290 The heat capacity and thermal expansion of bulk HAP and HAP-water  
nanoporous systems have been computed by means of MD simulations. These  
thermal properties are crucial to predict the thermo-mechanical behavior of  
bones and other HAP-rich materials. The simulations were used to assess the  
effects of temperature in bulk HAP and of confinement in HAP-water thermal  
295 properties. This work contributes towards a better understanding of the fac-  
tors affecting the thermo-mechanical behavior of bones. The identification of  
nanoscale phenomenon related to the confinement of water as a source of the  
property variability can be transferred to the study of other nanoporous ad-  
sorbing materials. As body fluid and natural water is rich in ions, further work  
300 will consider the role of dissolved ions in confined water and their effect on the  
macroscopic thermal properties of HAP-electrolyte systems.

## References

- [1] N. A. S. Taylor, M. J. Tipton, G. P. Kenny, Considerations for the mea-  
surement of core, skin and mean body temperatures, *Journal of Thermal*  
305 *Biology* 46 (2014) 72–101. doi:10.1016/j.jtherbio.2014.10.006.  
URL [http://www.sciencedirect.com/science/article/pii/  
S0306456514001521](http://www.sciencedirect.com/science/article/pii/S0306456514001521)
- [2] S. Karmani, The thermal properties of bone and the effects of  
surgical intervention, *Current Orthopaedics* 20 (1) (2006) 52–58.  
310 doi:10.1016/j.cuor.2005.09.011.  
URL [http://www.orthopaedicsandtraumajournal.co.uk/article/  
S0268-0890\(05\)00167-2/abstract](http://www.orthopaedicsandtraumajournal.co.uk/article/S0268-0890(05)00167-2/abstract)
- [3] W. R. Krause, D. W. Bradbury, J. E. Kelly, E. M. Lunceford, Temperature  
elevations in orthopaedic cutting operations, *Journal of Biomechanics*  
315 15 (4) (1982) 267–275. doi:10.1016/0021-9290(82)90173-7.

URL [http://www.sciencedirect.com/science/article/pii/0021929082901737](http://www.sciencedirect.com/science/article/pii/S0021929082901737)

[4] G. Augustin, T. Zigman, S. Davila, T. Udilljak, T. Staroveski, D. Brezak, S. Babic, Cortical bone drilling and thermal osteonecrosis, *Clinical Biomechanics* 27 (4) (2012) 313–325. doi:10.1016/j.clinbiomech.2011.10.010.

URL [http://www.clinbiomech.com/article/S0268-0033\(11\)00278-6/abstract](http://www.clinbiomech.com/article/S0268-0033(11)00278-6/abstract)

[5] E. B. Dolan, M. G. Haugh, D. Tallon, C. Casey, L. M. McNamara, Heat-shock-induced cellular responses to temperature elevations occurring during orthopaedic cutting, *Journal of The Royal Society Interface* 9 (77) (2012) 3503–3513. doi:10.1098/rsif.2012.0520.

URL <http://rsif.royalsocietypublishing.org/content/9/77/3503>

[6] R. L. Jacobs, R. D. Ray, The effect of heat on bone healing. A disadvantage in the use of power tools, *Archives of Surgery (Chicago, Ill.: 1960)* 104 (5) (1972) 687–691.

[7] E. Phillips, *Greek medicine*, Camelot Press Ltd, 1973.

[8] A. R. Eriksson, T. Albrektsson, Temperature threshold levels for heat-induced bone tissue injury: A vital-microscopic study in the rabbit, *The Journal of Prosthetic Dentistry* 50 (1) (1983) 101–107. doi:10.1016/0022-3913(83)90174-9.

URL <http://www.sciencedirect.com/science/article/pii/S0022391383901749>

[9] R. Calttenburg, J. Cohen, S. Conner, N. Cook, Thermal properties of cancellous bone, *Journal of Biomedical Materials Research Part A* 9 (2) (1975) 169–182. doi:10.1002/jbm.820090206.

URL <http://onlinelibrary.wiley.com/doi/10.1002/jbm.820090206/full>

- [10] S. Weiner, W. Traub, Organization of hydroxyapatite crystals within collagen fibrils, FEBS Letters 206 (2) (1986) 262–266.  
345
- [11] L. Kuhn, S. J. Eppell, W. Tong, M. J. Glimcher, J. L. Katz, Size and Shape of Mineralites in Young Bovine Bone Measured by Atomic Force Microscopy, Calcified Tissue International 72 (5) (2003) 592–598. doi:10.1007/s00223-002-1077-7.  
350 URL <http://link.springer.com/10.1007/s00223-002-1077-7>
- [12] J. M. Holmes, D. H. Davies, W. J. Meath, R. A. Beebe, Gas Adsorption and Surface Structure of Bone Mineral, Biochemistry 3 (12) (1964) 2019–2024. doi:10.1021/bi00900a042.  
URL <http://dx.doi.org/10.1021/bi00900a042>
- [13] I. Brovchenko, A. Oleinikova, Interfacial and Confined Water, Elsevier, 2008.  
355
- [14] F. M. Etzler, P. J. White, The heat capacity of water in silica pores, Journal of Colloid and Interface Science 120 (1) (1987) 94–99. doi:10.1016/0021-9797(87)90326-2.  
360 URL <http://www.sciencedirect.com/science/article/pii/0021979787903262>
- [15] F. M. Etzler, J. J. Connors, Temperature dependence of the heat capacity of water in small pores, Langmuir 6 (7) (1990) 1250–1253. doi:10.1021/la00097a010.  
365 URL <http://dx.doi.org/10.1021/la00097a010>
- [16] F. M. Etzler, R. F. Ross, R. A. Halcomb, The structure and properties of vicinal water: Lessons from statistical geometry, Physica A: Statistical Mechanics and its Applications 172 (1) (1991) 161–173. doi:10.1016/0378-4371(91)90318-7.  
370 URL <http://www.sciencedirect.com/science/article/pii/0378437191903187>

- [17] S. Xu, G. W. Scherer, T. S. Mahadevan, S. H. Garofalini, Thermal Expansion of Confined Water, *Langmuir* 25 (9) (2009) 5076–5083. doi:10.1021/la804061p.  
375 URL <http://dx.doi.org/10.1021/la804061p>
- [18] T. Honorio, B. Bary, F. Benboudjema, Thermal properties of cement-based materials: Multiscale estimations at early-age, *Cement and Concrete Composites* 87 (2018) 205–219. doi:10.1016/j.cemconcomp.2018.01.003.  
URL <http://www.sciencedirect.com/science/article/pii/S0958946516305200>  
380
- [19] M. J. A. Qomi, F.-J. Ulm, R. J.-M. Pellenq, Physical Origins of Thermal Properties of Cement Paste, *Physical Review Applied* 3 (6) (2015) 064010. doi:10.1103/PhysRevApplied.3.064010.  
URL <http://link.aps.org/doi/10.1103/PhysRevApplied.3.064010>
- 385 [20] T. Lemaire, J. Kaiser, S. Naili, V. Sansalone, Modelling of the transport in electrically charged porous media including ionic exchanges, *Mechanics Research Communications* 37 (5) (2010) 495–499. doi:10.1016/j.mechrescom.2010.05.009.  
URL <http://www.sciencedirect.com/science/article/pii/S0093641310000716>  
390
- [21] T. Honorio, T. Lemaire, D. Di Tommaso, S. Naili, Anomalous water and ion dynamics in hydroxyapatite mesopores, *Computational Materials Science*.
- [22] T. T. Pham, T. Lemaire, E. Capiiez-Lernout, M. Lewerenz, Q.-D. To, J. K. Christie, D. D. Tommaso, N. H. d. Leeuw, S. Naili, Properties of  
395 water confined in hydroxyapatite nanopores as derived from molecular dynamics simulations, *Theoretical Chemistry Accounts* 134 (5) (2015) 59. doi:10.1007/s00214-015-1653-3.  
URL <https://link.springer.com/article/10.1007/s00214-015-1653-3>

- 400 [23] M. Prakash, T. Lemaire, D. Di Tommaso, N. de Leeuw, M. Lewerenz,  
M. Caruel, S. Naili, Transport properties of water molecules confined  
between hydroxyapatite surfaces: A Molecular dynamics simula-  
tion approach, *Applied Surface Science* 418 (Part A) (2017) 296–301.  
doi:10.1016/j.apsusc.2017.02.029.
- 405 URL [http://www.sciencedirect.com/science/article/pii/  
S016943321730380X](http://www.sciencedirect.com/science/article/pii/S016943321730380X)
- [24] D. Di Tommaso, M. Prakash, T. Lemaire, M. Lewerenz, N. H. de Leeuw,  
S. Naili, Molecular Dynamics Simulations of Hydroxyapatite Nanopores in  
Contact with Electrolyte Solutions: The Effect of Nanoconfinement and  
410 Solvated Ions on the Surface Reactivity and the Structural, Dynamical,  
and Vibrational Properties of Water, *Crystals* 7 (2) (2017) 57. doi:10.  
3390/cryst7020057.
- URL <http://www.mdpi.com/2073-4352/7/2/57>
- [25] M. Prakash, T. Lemaire, M. Caruel, M. Lewerenz, N. H. d. Leeuw,  
415 D. D. Tommaso, S. Naili, Anisotropic diffusion of water molecules in  
hydroxyapatite nanopores, *Physics and Chemistry of Minerals* 44 (7)  
(2017) 509–519. doi:10.1007/s00269-017-0878-1.
- URL [https://link.springer.com/article/10.1007/  
s00269-017-0878-1](https://link.springer.com/article/10.1007/s00269-017-0878-1)
- 420 [26] G. Leibfried, W. Ludwig, Theory of Anharmonic Effects in Crystals, in:  
F. Seitz, D. Turnbull (Eds.), *Solid State Physics*, Vol. 12, Academic Press,  
1961, pp. 275–444. doi:10.1016/S0081-1947(08)60656-6.
- URL [http://www.sciencedirect.com/science/article/pii/  
S0081194708606566](http://www.sciencedirect.com/science/article/pii/S0081194708606566)
- 425 [27] T. Cagin, N. Karasawa, S. Dasgupta, W. A. Goddard, Thermodynamic and  
elastic properties of polyethylene at elevated temperatures, *MRS Online  
Proceedings Library Archive* 278.

- [28] T. Lee, Monte Carlo Simulations of Structural Phase Transitions in Metals and Alloys, PhD Thesis, Brown University (2010).
- 430 [29] J. R. Ray, A. Rahman, Statistical ensembles and molecular dynamics studies of anisotropic solids. II, *The Journal of Chemical Physics* 82 (9) (1985) 4243–4247. doi:10.1063/1.448813.  
URL <http://extranet.enpc.fr:3588/doi/abs/10.1063/1.448813>
- [30] J. R. Ray, Molecular dynamics equations of motion for systems varying in  
435 shape and size, *The Journal of Chemical Physics* 79 (10) (1983) 5128–5130.  
doi:10.1063/1.445636.  
URL <http://extranet.enpc.fr:3588/doi/abs/10.1063/1.445636>
- [31] D. C. Wallace, *Thermodynamics of Crystals*, Courier Corporation, 1998,  
google-Books-ID: qLzOmwSgMISc.
- 440 [32] M. P. Allen, D. J. Tildesley, *Computer Simulation of Liquids*, Oxford University Press, New York, 1989.
- [33] K. Sudarsanan, R. A. Young, Significant precision in crystal structural details. Holly Springs hydroxyapatite, *Acta Crystallographica Section B: Structural Crystallography and Crystal Chemistry* 25 (8) (1969) 1534–1543.  
445 doi:10.1107/S0567740869004298.  
URL <http://scripts.iucr.org/cgi-bin/paper?a06841>
- [34] D. Mkhonto, N. H. d. Leeuw, A computer modelling study of the effect of water on the surface structure and morphology of fluorapatite: introducing a  $\text{Ca}_{10}(\text{PO}_4)_6\text{F}_2$  potential model, *Journal of Materials Chemistry* 12 (9)  
450 (2002) 2633–2642. doi:10.1039/B204111A.  
URL <http://pubs.rsc.org/en/content/articlelanding/2002/jm/b204111a>
- [35] N. H. de Leeuw, A computer modelling study of the uptake and segregation of fluoride ions at the hydrated hydroxyapatite (0001) surface: introducing  
455 a  $\text{Ca}_{10}(\text{PO}_4)_6(\text{OH})_2$  potential model, *Physical Chemistry Chemical*

Physics 6 (8) (2004) 1860–1866. doi:10.1039/B313242K.

URL <http://pubs.rsc.org/en/Content/ArticleLanding/2004/CP/B313242K>

[36] N. H. de Leeuw, S. C. Parker, Molecular-dynamics simulation of MgO surfaces in liquid water using a shell-model potential for water, Physical Review B 58 (20) (1998) 13901–13908. doi:10.1103/PhysRevB.58.13901.

URL <https://link.aps.org/doi/10.1103/PhysRevB.58.13901>

[37] H. J. C. Berendsen, J. R. Grigera, T. P. Straatsma, The missing term in effective pair potentials, The Journal of Physical Chemistry 91 (24) (1987) 6269–6271. doi:10.1021/j100308a038.

URL <http://dx.doi.org/10.1021/j100308a038>

[38] N. Almora-Barrios, N. H. d. Leeuw, Modelling the interaction of a Hyp-Pro-Gly peptide with hydroxyapatite surfaces in aqueous environment, CrystEngComm 12 (3) (2010) 960–967. doi:10.1039/B917179G.

URL <https://pubs.rsc.org/en/content/articlelanding/2010/ce/b917179g>

[39] S. E. R. Hernandez, I. Streeter, N. H. d. Leeuw, The effect of water on the binding of glycosaminoglycan saccharides to hydroxyapatite surfaces: a molecular dynamics study, Physical Chemistry Chemical Physics 17 (34) (2015) 22377–22388. doi:10.1039/C5CP02630J.

URL <https://pubs.rsc.org/en/content/articlelanding/2015/cp/c5cp02630j>

[40] I. T. Todorov, W. Smith, K. Trachenko, M. T. Dove, DL\_poly\_3 new dimensions in molecular dynamics simulations via massive parallelism, Journal of Materials Chemistry 16 (20) (2006) 1911–1918. doi:10.1039/B517931A.

URL <http://pubs.rsc.org/en/content/articlelanding/2006/jm/b517931a>

[41] J. R. Ray, Elastic constants and statistical ensembles in molecular dynamics, Computer Physics Reports 8 (3) (1988) 109–151.

- 485 doi:10.1016/0167-7977(88)90009-3.  
URL <http://www.sciencedirect.com/science/article/pii/0167797788900093>
- [42] T. Honorio, L. Brochard, M. Vandamme, Hydration Phase Diagram of Clay Particles from Molecular Simulations, *Langmuir* 33 (44) (2017) 12766–  
490 12776. doi:10.1021/acs.langmuir.7b03198.  
URL <http://dx.doi.org/10.1021/acs.langmuir.7b03198>
- [43] M. Parrinello, A. Rahman, Strain fluctuations and elastic constants, *The Journal of Chemical Physics* 76 (5) (1982) 2662–2666. doi:10.1063/1.443248.  
495 URL <http://aip.scitation.org/doi/abs/10.1063/1.443248>
- [44] T. Kijima, M. Tsutsumi, Preparation and Thermal Properties of Dense Polycrystalline Oxyhydroxyapatite, *Journal of the American Ceramic Society* 62 (9-10) (1979) 455–460. doi:10.1111/j.1151-2916.1979.tb19104.x.  
500 URL <http://onlinelibrary.wiley.com/doi/10.1111/j.1151-2916.1979.tb19104.x/abstract>
- [45] E. P. Egan, Z. T. Wakefield, K. L. Elmore, High-Temperature Heat Content of Hydroxyapatite, *Journal of the American Chemical Society* 72 (6) (1950) 2418–2421. doi:10.1021/ja01162a019.  
505 URL <https://doi.org/10.1021/ja01162a019>
- [46] F. J. A. L. Cruz, J. N. Canongia Lopes, J. C. G. Calado, M. E. Minas da Piedade, A Molecular Dynamics Study of the Thermodynamic Properties of Calcium Apatites. 1. Hexagonal Phases, *The Journal of Physical Chemistry B* 109 (51) (2005) 24473–24479. doi:10.1021/jp054304p.  
510 URL <http://dx.doi.org/10.1021/jp054304p>
- [47] S. Nakamura, R. Otsuka, H. Aoki, M. Akao, N. Miura, T. Yamamoto, Thermal expansion of hydroxyapatite–tricalcium phosphate ceramics, *Thermochimica Acta* 165 (1) (1990) 57–72.

doi:10.1016/0040-6031(90)80206-E.

515 URL <http://www.sciencedirect.com/science/article/pii/004060319080206E>

[48] F. J. A. L. Cruz, J. N. Canongia Lopes, J. C. G. Calado, Molecular Dynamics Study of the Thermodynamic Properties of Calcium Apatites. 2. Monoclinic Phases, *The Journal of Physical Chemistry B* 110 (9) (2006) 4387–4392. doi:10.1021/jp055808q.

520 URL <https://doi.org/10.1021/jp055808q>

[49] W. Y. Ching, P. Rulis, A. Misra, Ab initio elastic properties and tensile strength of crystalline hydroxyapatite, *Acta Biomaterialia* 5 (8) (2009) 3067–3075. doi:10.1016/j.actbio.2009.04.030.

525 URL <http://www.sciencedirect.com/science/article/pii/S1742706109001949>

[50] R. Snyders, D. Music, D. Sigumonrong, B. Schelnberger, J. Jensen, J. M. Schneider, Experimental and ab initio study of the mechanical properties of hydroxyapatite, *Applied Physics Letters* 90 (19) (2007) 193902. doi:10.1063/1.2738386.

530 URL <http://aip.scitation.org/doi/abs/10.1063/1.2738386>

[51] R. F. S. Hearmon, A. A. Maradudin, An Introduction to Applied Anisotropic Elasticity, *Physics Today* 14 (1961) 48. doi:10.1063/1.3057153.

535 URL <http://adsabs.harvard.edu/abs/1961PhT...14j..48H>

[52] S. Lees, F. Rollins Jr., Anisotropy in hard dental tissues, *Journal of Biomechanics* 5 (6) (1972) 557–564. doi:10.1016/0021-9290(72)90027-9.

URL <http://www.sciencedirect.com/science/article/pii/0021929072900279>

540 [53] R. S. Gilmore, J. L. Katz, Elastic properties of apatites, *Journal of Materials Science* 17 (4) (1982) 1131–1141. doi:10.1007/BF00543533.

URL <https://link.springer.com/article/10.1007/BF00543533>

- [54] J. S. Dugdale, D. K. C. MacDonald, The Thermal Expansion of Solids, Physical Review 89 (4) (1953) 832–834. doi:10.1103/PhysRev.89.832.  
545 URL <https://link.aps.org/doi/10.1103/PhysRev.89.832>
- [55] G. Grimvall, Thermophysical Properties of Materials, Elsevier, 1999, google-Books-ID: jfP4CePrv6QC.
- [56] I. Lifshitz, Thermal properties of chain and layered structures at low temperatures, Zh. Eksp. Teor. Fiz 22 (4) (1952) 475–486.
- 550 [57] J. Fabian, P. B. Allen, Thermal Expansion and Gruneisen Parameters of Amorphous Silicon: A Realistic Model Calculation, Physical Review Letters 79 (10) (1997) 1885–1888. doi:10.1103/PhysRevLett.79.1885.  
URL <https://link.aps.org/doi/10.1103/PhysRevLett.79.1885>
- [58] N. A. Abdullaev, Gruneisen parameters for layered crystals, Physics of the  
555 Solid State 43 (4) (2001) 727–731. doi:10.1134/1.1366002.  
URL <https://doi.org/10.1134/1.1366002>
- [59] Y. Mao, Y. Zhang, Thermal conductivity, shear viscosity and specific heat of rigid water models, Chemical Physics Letters 542 (2012) 37–41. doi:10.1016/j.cplett.2012.05.044.  
560 URL <http://www.sciencedirect.com/science/article/pii/S0009261412006367>
- [60] G. R. Fischer, P. Bardhan, J. E. Geiger, The lattice thermal expansion of hydroxyapatite, Journal of Materials Science Letters 2 (10) (1983) 577–578. doi:10.1007/BF00719864.  
565 URL <https://link.springer.com/article/10.1007/BF00719864>
- [61] G. J. Dvorak, Y. Benveniste, On Transformation Strains and Uniform Fields in Multiphase Elastic Media, Proceedings of the Royal Society of London A: Mathematical, Physical and Engineering Sciences 437 (1900) (1992) 291–310. doi:10.1098/rspa.1992.0062.

570 URL <http://rspa.royalsocietypublishing.org/content/437/1900/291>

[62] R. deWit, Elastic constants and thermal expansion averages of a nontextured polycrystal, *Journal of Mechanics of Materials and Structures* 3 (2) (2008) 195–212. doi:10.2140/jomms.2008.3.195.

575 URL <https://msp.org/jomms/2008/3-2/p01.xhtml>